International Symposium
On Turbulence and Shear Flow
Phenomena (TSFP-9)
June 30 - July 3, 2015 *Melbourne, Australia*

WAKE STRUCTURE OF A SINGLE VERTICAL AXIS WIND TURBINE

Antonio Posa
Department of Mechanical and Aerospace Engineering
George Washington University
800 22nd St, NW, Washington, DC 20052, USA
aposa@email.gwu.edu

Colin Parker
Department of Mechanical and Aerospace Engineering
George Washington University
800 22nd St, NW, Washington, DC 20052, USA
colinparker@gwu.edu

Megan C. Leftwich
Department of Mechanical and Aerospace Engineering
George Washington University
800 22nd St, NW, Washington, DC 20052, USA
mleftwich@gwu.edu

Elias Balaras
Department of Mechanical and Aerospace Engineering
George Washington University
800 22nd St, NW, Washington, DC 20052, USA
balaras@gwu.edu

ABSTRACT

The wake structure behind a vertical axis wind turbine (VAWT) is both measured using a scaled model in a wind tunnel and computed by means of large-eddy simulation (LES). The experiment is done using stereo particle imaging velocimetry (sPIV) at the mid-plane of the model, allowing the in-plane velocity field (streamwise u_z and cross-stream u_x components) as well as the out of plane velocity (u_y) to be measured. The dependence of the wake structure on the Tip Speed Ratio, TSR, is studied, showing higher asymmetry and coherence at the lower rotational speed, due to stronger dynamic stall phenomena, affecting especially the leeward side of the wake. This behavior differs from that in the wake of a spinning cylinder, frequently adopted to model this class of turbines. Both instantaneous and averaged fields are discussed.

INTRODUCTION

Most of the wind energy around the world today is produced by horizontal axis wind turbines (HAWTs), which make up the majority of wind farms. Despite the constant development and design improvements, the spacing required between HAWTs limits the overall farm efficiency per unit area. Therefore, large wind farms need significant land and wind resources, available in remote rural regions and not near cities, which comprise the majority of a country's energy demand, resulting in distribution issues. VAWTs are attractive small-scale turbines, as they offer various advantages over small-scale HAWTs for installation in urban and suburban areas: they are independent of wind direction and can produce power under lower wind speeds; furthermore their dimensions, aesthetic appeal and virtually noiseless nature reduce their environmental impact, making them more acceptable by local communities.

Recent field testing demonstrated that VAWTs can be spaced closer together, when compared to typical HAWTs, resulting potentially in higher power densities (Dabiri, 2011). In particular, velocity measurements in an array of VAWTs revealed that a distance of approximately 6 diameters was required to recover 95% of the upwind velocity, compared to 14 needed by HAWTs (Kinzel *et al.*, 2012). It was also shown that closely spaced counter-rotating VAWTs pairs had higher efficiency than two isolated turbines. To understand these phenomena, as well as optimize the arrangement of VAWTs in a large farm, typically their wakes are assumed to resemble those of rotating cylinders (Dabiri, 2011). However, the geometry of a VAWT is more complex than that of a spinning cylinder: unlike a cylinder, the turbine has a cross-section that

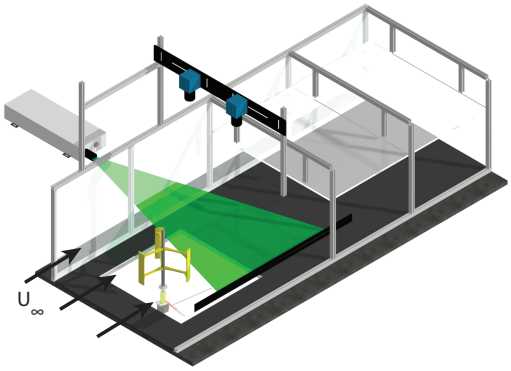

Figure 1. The experiments are conducted with a scale model of the VAWT in an open wind tunnel. In all cases, $Re_D = 180{,}00$ and TSR is either $TRS_1 = 1.35$ or $TRS_2 = 2.21$.

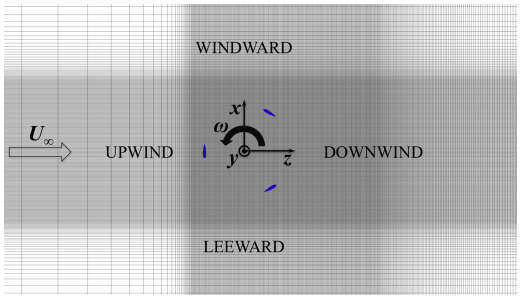

Figure 2. Representation of a slice of the computational grid orthogonal to the axis of the turbine (for clarity, only 1 every 4 nodes is plotted along both directions). The hollow arrow shows the direction of the free-stream, the solid arrow that of the turbine rotation.

is mostly open, with a smaller solidity. Each turbine airfoil sheds a leading and trailing edge vortex as the turbine rotates. Also the Reynolds numbers of full-scale VAWT systems are typically orders of magnitude larger than those of previous studies in the literature on rotating cylinders (Yoon *et al.*, 2009; Chan *et al.*, 2011).

In this study we will expand upon current knowledge using closely coordinated experiments and computations to characterize the wake behind an isolated VAWT. Both geometry and working conditions are closely matched to typical VAWTs applications.

METHODS

This work uses carefully coordinated experiments and computations. In both the turbine geometry is based on the design proposed by Howell *et al.*, 2010. Its rotor is composed of three NACA0022 airfoils. The ratio of the rotor diameter, D, to the the chord length, c, is $D/c = 6$. The Reynolds number, Re_D, based on D and the free-stream velocity, U_∞, is 180,000 in both computations and experiments. The working conditions of a VAWT are characterized by its Tip Speed Ratio, that is the ratio between the tangential velocity of the turbine blades and the free-stream velocity, $TSR = \omega D/U_\infty$, where ω is the rotational speed. Two Tip Speed Ratios are tested here: $TSR_1 = 1.35$ and $TSR_2 = 2.21$, to investigate the sensitivity of the wake properties to this parameter.

Experimental setup

The wind tunnel testing is done using sPIV at the midplane behind a scaled model VAWT. The model is driven at constant rotational speed to the desired TSR. In an open-ended wind tunnel the model is mounted 0.6 [m] downstream of the inlet of a 0.38 (spanwise) $\times$ 0.91 (cross-stream) $\times$ 2.44 [m] (streamwise) test section. The height of the model along the span is equal to 0.20 [m]. A laser sheet is directed through optical glass on the side of the tunnel in a plane parallel to the free-stream. The roof of the test section is optically clear, allowing the cameras to capture the illuminated plane from above. A schematic of the experimental setup is shown in Figure 1. An infrared sensor is used to measure each rotation of the turbine. That signal is processed by the programmable timing unit (PTU) to trigger the sPIV system at specific positions. By taking multiple images at each position we can get phase-averaged velocity fields. Each phase-averaged image is derived from 100 instantaneous velocity fields.

Computational method

A LES approach is adopted here: the large eddies are accurately computed without any assumption on the properties of the large-scale turbulence, which is beneficial to the accuracy of the solution. All computations are conducted on staggered Cartesian grids, utilizing central finite-differences for the discretization of the derivatives in space. The filtered Navier-Stokes equations are advanced in time using a fractional-step method, as discussed, for instance, by Van Kan, 1986. To enforce boundary conditions on the rotating airfoils, which do not conform to the grid, an immersed-boundary formulation is used. The details on the computational approach, together with extensive validation in laminar and turbulent flows, can be found in Balaras, 2004, Yang & Balaras, 2006 and Vanella *et al.*, 2014. The turbine model is the same as that considered in the experiments. However in the computations periodic conditions are utilized along the spanwise direction, which implies that the end effects are not taken into account in the present simulations. At the inlet of the computational domain a uniform velocity, U_∞, is enforced; at the lateral boundaries a slip-wall condition is adopted; at the outflow a convective condition (Orlanski, 1976) allows the perturbations leaving the computational domain. The turbine axis is placed at $5D$ downstream of the inlet, $10D$ upstream of the outlet and $5D$ from the cross-stream boundaries of the domain, whose spanwise extent is equivalent to 4 chord lengths in the simulations discussed in the present paper. The Cartesian grid is uniform in the region spanned by the turbine rotor and is stretched away from it, but keeping an adequate level of resolution up to 5 diameters downstream of its axis, in order to simulate properly the evolution of the wake structures. The resolution in the rotor region is equivalent to $0.01c$ along each direction in space. A simplified representation of a slice of the computational grid, orthogonal to the axis of the turbine, is provided in Figure 2, where also the nomenclature adopted in the following discussion is introduced, together with the adopted reference frame.

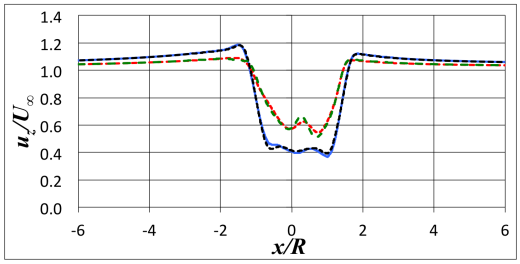

(a)

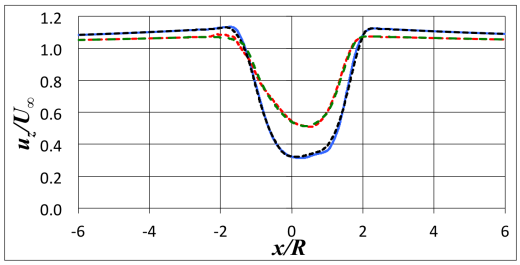

(b)

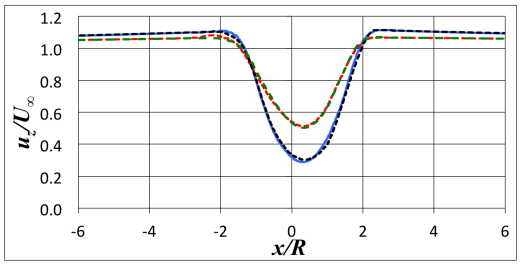

(c)

Figure 3. Cross-stream profiles of the streamwise velocity component u_z at 1 (a), 3 (b) and 5 (c) diameters downstream of the turbine axis. The profiles are extracted from the ensemble-averaged fields and are non-dimensionalized by the free-stream velocity and the radius of the turbine. The lines refer respectively to: higher TSR & smaller domain (———), lower TSR & smaller domain (- - -), higher TSR & larger domain (– – –) and lower TSR & larger domain (– – –).

RESULTS

The effect of the TSR on the time-averaged streamwise velocity component is represented in Figure 3 by means of the cross-stream profiles at 1, 3 and 5 diameters downstream of the axis of the turbine, extracted from the LES fields. They have been averaged in time over 10 rotations of the turbine and across the spanwise periodic dimension of the domain. The plots in Figure 3 are scaled using the free-stream velocity and the radius of the rotor, R. In comparison with the simulations reported by Barsky *et al.*, 2014 for a spanwise extent of the computational domain equivalent to 2 chord lengths (smaller domain), the agreement of the present ones (larger domain), using 4 chord lengths, is very close. Therefore a displacement of the momentum deficit towards the windward side (positive x coordinates) is confirmed, which matches qualitatively the behavior in the wake of a spinning cylinder. It is remarkable the streamwise increase of the momentum deficit in the near wake, also observed in the recent PIV experiments by Tescione *et al.*, 2014, which is due to the diffusion downstream of the structures generated by the stall of the blades during their downwind trajectory, populating the core of the wake. These structures are stronger at the lower TSR. They cause a local peak for $TSR_1 = 1.35$ and a plateau for $TSR_2 = 2.21$ at the first streamwise location, as shown in Figure 3(a): the angles of attack experienced by the blades are larger at the lower TSR, which entails stronger separation phenomena and larger coherent structures. The above behavior in the core of the wake is in well qualitative agreement with the results of the LDV experiments by Fraunié *et al.*, 1986, although carried out at a much smaller Reynolds number $Re_D = 10,000$. They also observed a local maximum of streamwise velocity, higher at lower values of TSR. Note also that in Figure 3 the momentum deficit is larger at the higher TSR, since a higher rotational speed is equivalent to a higher solidity: in other words, the behavior of the turbine wake gets closer to that of a spinning cylinder. Moving downstream the wake becomes more symmetric, but keeping an off-set of its axis.

An example of the experimentally measured wake structure for TSR_1 is shown in Figure 4, where the out of plane component of the phase-averaged vorticity is plotted at the mid-span directly behind the model. Clearly the large-scale vortices in the wake correlate with the position of the turbine blades and are associated with the stall during their downwind motion. As the turbine blades enters the downstream section of its cycle, there is a strong vortex attached to the blade with a trailing vortex sheet. As the blade progresses and turns back upstream, the vortex is shed and moves downstream.

In Figure 5 the ensemble-averaged fields of turbulent kinetic energy from the simulations at the lower (a) and the higher (b) $TSRs$ are shown. Again, they are estimated by means of an average in time and along the spanwise direction. We see that a lower TSR, associated with larger angles of attack, implies higher values of turbulent kinetic energy in the rotor region, due to a stronger stall of the blades, affecting especially the leeward side of the rotor (negative x coordinates). At both $TSRs$ the wake is characterized by higher turbulence at its edges. On the leeward side this is caused by the stall of the blades during their upwind motion, while on the windward side by the shear layer shed by the blades when they travel on the upper part of their trajectory, experiencing lower values of angle of attack: therefore the turbulent kinetic energy is higher at the bottom edge of the wake in both panels of Figure 5. Once again, we found this result in qualitative agreement with those by Fraunié *et al.*, 1986 and the more recent ones by acoustic Doppler velocimetry reported by Bachant *et al.*, 2015. Furthermore the lower TSR case highlights the presence of an additional region of high turbulence in the near wake, populating its core and produced by the stall of the blades during their downwind motion. This fades out more quickly than that on the leeward edge of the wake, since the structures originated by the downwind stall lose their coherence over a shorter distance downstream. It is obvious that the pattern shown in Figure 5 differs from that in the wake of a spinning cylinder: in the present case the main unsteady activity is observed on the leeward side, while for a spinning cylinder the vortex shedding displays the same displacement of the momentum deficit.

The important role of the downwind stall at the lower TSR, shown by both Figure 3 and Figure 5, was confirmed by the PIV measurements in the near wake of the turbine.

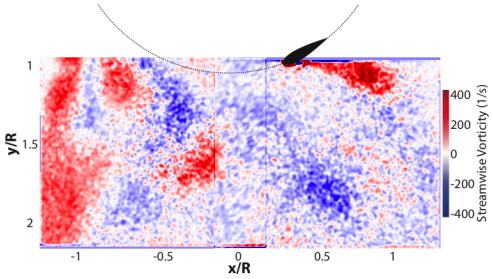

(a)

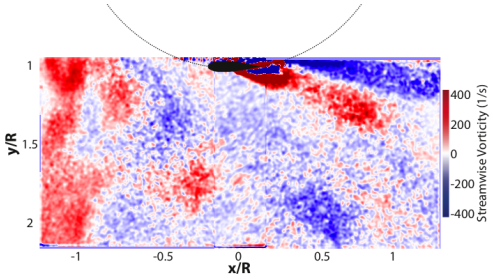

(b)

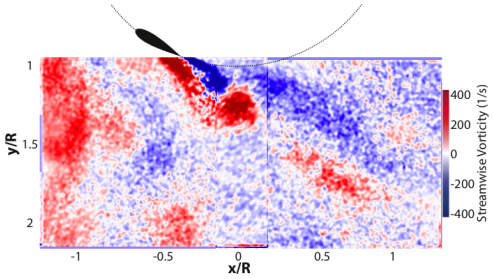

(c)

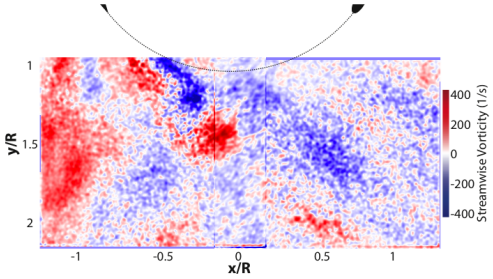

(d)

Figure 4. Out of plane phase-averaged vorticity with $Re_D = 180{,}000$ and $TSR = 1.35$. The turbine rotation is clockwise with the free-stream from top to bottom. One third cycle is shown, progressing from (a) to (d) in increments of 30 degrees.

In the present experiments the window was located immediately downstream of the rotor trajectory and spanned a cross-stream extent equal to approximately 1 turbine diameter; therefore it was especially suitable to identify the presence of the vortices produced by the downwind stall of the blades, populating the central region of the near wake. In the future we plan to extend the experimental window along both the cross-stream and streamwise directions. In

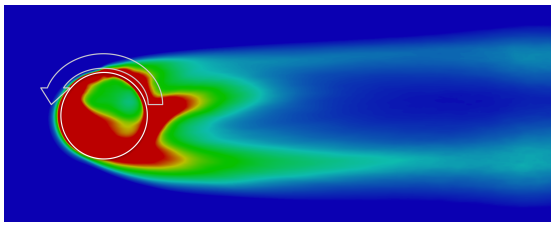

(a)

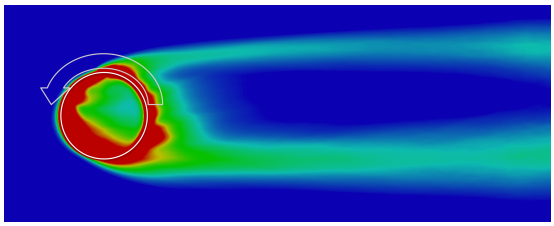

(b)

Figure 5. Ensemble-averaged fields of turbulent kinetic energy sampled in time (10 revolutions) and along the homogeneous spanwise direction at the lower (top) and the higher (bottom) values of TSR. The scale ranges from 0 (blue) to 0.1 (red). The fields are non-dimensionalized by the square of the free-stream velocity. The trajectory of the blades and the direction of their motion are represented.

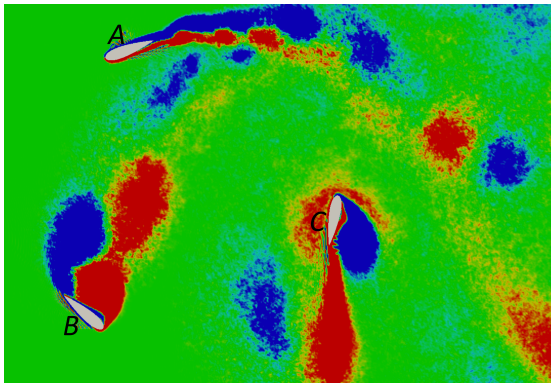

(a)

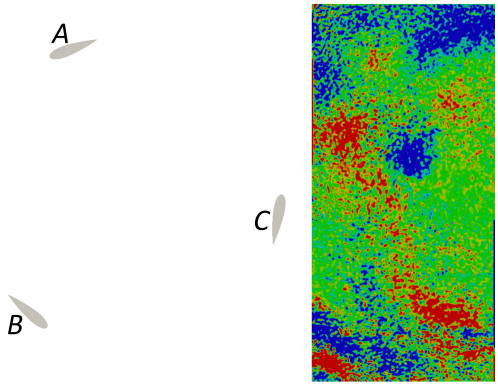

(b)

Figure 6. Phase-averaged fields of spanwise vorticity at the lower $TSR = TSR_1$ from LES computations (a) and PIV experiments (b). The scale ranges from -5 (blue) to 5 (red). The fields are non-dimensionalized by U_∞/D.

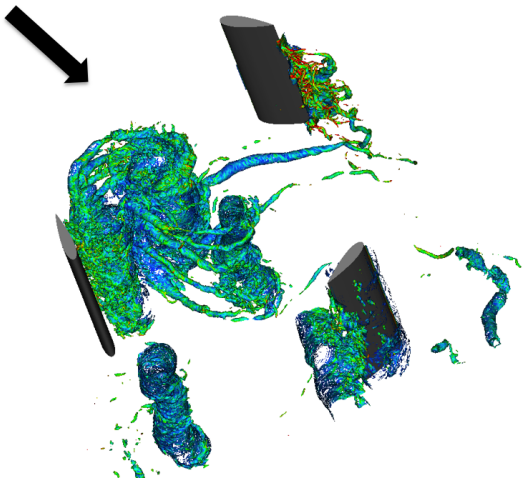

(a)

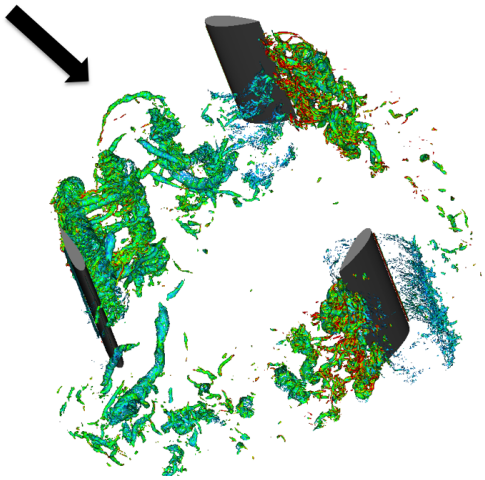

(b)

Figure 7. Instantaneous isosurfaces of pressure, colored by the vorticity magnitude: (a) lower TSR; (b) higher TSR. The arrow shows the direction of the free-stream.

Figure 6 a comparison of the phase-averaged fields of spanwise vorticity is presented between computations and experiments at $TSR_1 = 1.35$. Note that the represented extent of the domain is larger than the actual one of the experimental window, in order to show the particular rotor configuration relative to the phase-averaged fields in Figure 6. The qualitative agreement between computations and experiments is good. A pair of structures is distinguishable at about the center of the turbine near wake in both (a) and (b): they were produced by the downwind stall of the preceding blade A. Observe also that from that location up to the bottom right corner of Figure 6 the footprint of the wake of the same blade A is shown by a region of positive spanwise vorticity. Actually, the strong peak located at the bottom right corner is reinforced by the upwind stall, as we will discuss in more details later, looking at additional phase-averaged fields from the computations. Also in the experimental results the presence of large structures at the edge of the overall wake is detected, which agrees with the upper and lower peaks of turbulent kinetic energy seen in Figure 5.

Some three-dimensional snapshots from the LES computations are useful to develop a better insight about the

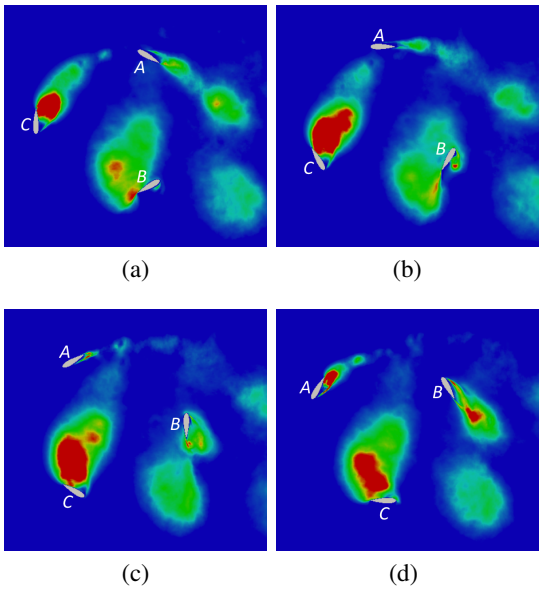

(a) (b)

(c) (d)

Figure 8. Phase-averaged turbulent kinetic energy at the lower TSR, scaled by the square of the free-stream velocity. The color fields range from 0 (blue) to 0.1 (red). The 4 rotor positions are 30° apart.

topology of the structures populating the rotor region and the wake of the turbine. In Figure 7 instantaneous isosurfaces of pressure, colored by the vorticity magnitude, are utilized to identify the structures produced by stall phenomena. At the lower TSR in Figure 7(a) the spanwise coherence is much stronger than that at the higher TSR in Figure 7(b). Large rollers are visible, associated especially with the upwind stall. Also elongated structures in the plane of the main flow are detected, connecting the spanwise rollers. Similar phenomena are observed at the higher TSR in Figure 7(b), but the vortices are less coherent and smaller, because of the smaller angles of attack experienced by the blades. For instance, whereas in Figure 7(a) a large roller is still visible in the bottom part of the figure, due to earlier stall phenomena, the level of coherence is reduced in the same region of Figure 7(b). Especially at the lower TSR the asymmetry of the field is evident, with larger vortices populating the leeward side of the rotor, compared to the windward side. This asymmetry is consistent with the results of the LES study carried out by Li *et al.*, 2013, who also observed big rollers produced in the same region of the blades trajectory.

Some more details relative to the wake of each airfoil and its role in the overall turbine wake have been extracted from the phase-averaged fields of turbulent kinetic energy, where the average is again performed along the spanwise direction and in time, but for specific rotor positions. The comparison of 4 different configurations in Figure 8 and in Figure 9 for the lower and the higher $TSRs$ respectively allows us to show the sensitivity to the value of TSR. In Figure 8 the wake of each airfoil is larger than in Figure 9, since the angles of attack seen by each blade are larger too. Note also that in the upwind region the stall is stronger than in the downwind one. Indeed downwind the induced velocity is lower than the free-stream, which increases the actual value of TSR and decreases the angles of attack experienced by the blades. Again, the asymmetry of the flow field along the

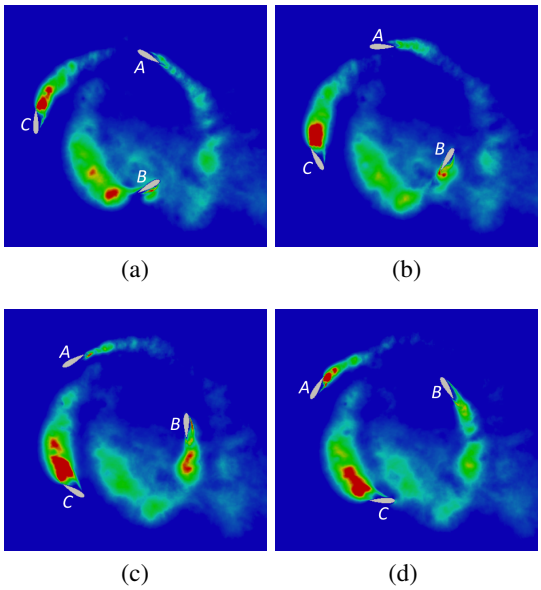

(a) (b) (c) (d)

Figure 9. Phase-averaged turbulent kinetic energy at the higher TSR, scaled by the square of the free-stream velocity. The color fields range from 0 (blue) to 0.1 (red). The 4 rotor positions are 30° apart.

cross-stream direction is evident, with larger wakes on the leeward side than on the windward one, affecting substantially the properties of the overall wake of the turbine downstream, as discussed above. Furthermore, at the lower TSR each blade interacts more with its own wake than with that shed by other airfoils. For instance, in Figure 8(a) and Figure 8(b) the blade B is traveling through its own wake. This can be seen also looking at the blade C across the whole sequence shown in Figure 8: the blade C is "followed" by its wake, generated by its upwind stall. On the contrary, in Figure 9(a) and Figure 9(b) the blade B is moving through the wake shed earlier by the blade A and the entire sequence in Figure 9 shows that the blade C is approaching the wake of the blade B. Looking at the turbulence associated with both the upwind and downwind stall of the blades, it is also evident that the footprint of the wake of each airfoil in the overall wake of the turbine is reduced at this higher value of TSR.

CONCLUSIONS

The wake of an isolated vertical axis wind turbine was investigated by both LES computations and sPIV measurements for a value of the Reynolds number $Re_D = 180,000$ and two Tip Speed Ratios, equal to $TSR_1 = 1.35$ and $TSR_2 = 2.21$, respectively. The qualitative agreement between numerical and experimental results is good, especially at the lower TSR, for which the blockage generated by the turbine model spinning inside the wind tunnel was lower. More quantitative comparisons will be presented in future papers. The role of the TSR on the wake properties was studied. Lower $TSRs$ imply higher angles of attack experienced by the airfoils, with stronger dynamic stall phenomena, in both the upwind and downwind regions of the trajectory of the blades. As a consequence, although the momentum deficit of the wake is displaced towards the windward side, as for a spinning cylinder, the largest coherent structures are produced and move downstream on the leeward side. Therefore the highest turbulent fluctuations populate the latter side of the turbine wake. Additionally, the wake of each single blade was studied, showing that lower values of TSR cause a reduced interaction among airfoils and an increased interaction with their own wakes: in its downwind trajectory each blade moves through the structures generated by its own upwind stall.

REFERENCES

Bachant, P. & Wosnik, M. 2015 Characterising the near-wake of a cross-flow turbine. *Journal of Turbulence* **16** (4), 392–410.

Balaras, E. 2004 Modeling complex boundaries using an external force field on fixed Cartesian grids in large-eddy simulations. *Computers & Fluids* **33** (3), 375–404.

Barsky, D., Posa, A., Rahromostaqim, M., Leftwich, M. C. & Balaras, E. 2014 Experimental and computational wake characterization of a vertical axis wind turbine. In *AVIATION 2104, 32nd AIAA Applied Aerodynamics Conference, 16-20 June 2014, Atlanta*. AIAA.

Chan, A. S., Dewey, P. A., Jameson, A., Liang, C. & Smits, A. J. 2011 Vortex suppression and drag reduction in the wake of counter-rotating cylinders. *Journal of Fluid Mechanics* **679** (1), 343–382.

Dabiri, J. O. 2011 Potential order-of-magnitude enhancement of wind farm power density via counter-rotating vertical-axis wind turbine arrays. *Journal of Renewable and Sustainable Energy* **3**, 043104.

Fraunié, P., Béguier, C., Paraschivoiu, I. & Brochier, G. 1986 Water channel experiments of dynamic stall on darrieus wind turbine blades. *Journal of Propulsion and Power* **2** (5), 445–449.

Howell, R., Qin, N., Edwards, J. & Durrani, N. 2010 Wind tunnel and numerical study of a small vertical axis wind turbine. *Renewable Energy* **35** (2), 412–422.

Kinzel, M., Mulligan, Q. & Dabiri, J. O. 2012 Energy exchange in an array of vertical-axis wind turbines. *Journal of Turbulence* **13** (1).

Li, C., Zhu, S., Xu, Y. L. & Xiao, Y. 2013 2.5 D large eddy simulation of vertical axis wind turbine in consideration of high angle of attack flow. *Renewable energy* **51**, 317–330.

Orlanski, I. 1976 A simple boundary condition for unbounded hyperbolic flows. *Journal of Computational Physics* **21** (3), 251–269.

Tescione, G., Ragni, D., He, C., Ferreira, C. S. & van Bussel, G. J. W. 2014 Near wake flow analysis of a vertical axis wind turbine by stereoscopic particle image velocimetry. *Renewable Energy* **70**, 47–61.

Van Kan, J. J. I. M. 1986 A second-order accurate pressure-correction scheme for viscous incompressible flow. *SIAM Journal on Scientific and Statistical Computing* **7** (3), 870–891.

Vanella, M., Posa, A. & Balaras, E. 2014 Adaptive Mesh Refinement for Immersed Boundary Methods. *Journal of Fluids Engineering* **136** (4), 040909–1,9.

Yang, J. & Balaras, E. 2006 An embedded-boundary formulation for large-eddy simulation of turbulent flows interacting with moving boundaries. *Journal of Computational Physics* **215** (1), 12–40.

Yoon, H. S., Chun, H. H., Kim, J. H. & Ryong Park, I. L. 2009 Flow characteristics of two rotating side-by-side circular cylinder. *Computers & Fluids* **38** (2), 466–474.